Direct Reservoir Parameter Estimation Using Joint Inversion of Marine Seismic AVA & CSEM Data

G. Michael Hoversten[1], Florence Cassassuce[1], Erika Gasperikova[1], Gregory A. Newman[1], Yoram Rubin[2], Zhangshuan, Hou[2], and Don Vasco[1]

[1] *Lawrence Berkeley National Laboratory*
[2] *University of California at Berkeley*

Abstract

A new joint inversion algorithm to directly estimate reservoir parameters is described. This algorithm combines seismic amplitude versus angle (AVA) and marine controlled source electromagnetic (CSEM) data. The rock-properties model needed to link the geophysical parameters to the reservoir parameters is described. Errors in the rock-properties model parameters, measured in percent, introduce errors of comparable size in the joint inversion reservoir parameter estimates. Tests of the concept on synthetic one-dimensional models demonstrate improved fluid saturation and porosity estimates for joint AVA-CSEM data inversion (compared to AVA or CSEM inversion alone). Comparing inversions of AVA, CSEM, and joint AVA-CSEM data over the North Sea Troll field, at a location with well control, shows that the joint inversion produces estimated gas saturation, oil saturation and porosity that is closest (as measured by the RMS difference, L1 norm of the difference, and net over the interval) to the logged values whereas CSEM inversion provides the closest estimates of water saturation.

Introduction

The estimation of reservoir parameters from geophysical data is the goal of most geophysical surveys performed in the context of hydrocarbon exploration and production. In recent years the focus has been on the use of time-lapse seismic data for predicting changes in pressure and fluid saturation (Tura and Lumley, 1999; Landro, 2001; Lumley et al., 2003). Predictions of changes in pore pressure (P_p) and water saturation (S_w) can be done when there is only oil saturation (S_o) and S_w, since there are only two independent variables, P_p and either S_w or S_o (S_o+S_w = 1), to be derived from two data (acoustic impedance and shear impedance). The presence of gas complicates the problem by introducing a third independent variable, gas saturation (S_g) which causes, for example, the change in S_o as a function of the change in shear and acoustic impedance to become multivalued.

Another interesting case arises in the exploration for economic gas deposits, where determining the level of S_g is critical. While the amplitude of reflections as a function of the source-receiver offset (AVO), or versus angle (AVA), can be used to estimate S_w and S_o, its use for S_g is more problematic. The state of affairs for seismic gas exploration using AVO was summarized by Castagna (1993): "According to Gassmann's equations, a gas sand with 1 percent gas saturation can have the same V_p/V_s as a commercial accumulation of gas. Thus, unless

density can be very accurately extracted utilizing far offset information, AVO cannot distinguish commercial and noncommercial gas accumulations." Subsequent research on the inversion of AVA data to predict seismic parameters (Debski and Tarantola, 1995; Drufuca and Mazzotti, 1995; Plessix et al., 2000; Buland and More, 2003) has concluded that density is the least well-determined parameter in any form of AVA inversion and cannot be reliably estimated for practical purposes. Thus, current seismic technology cannot reliably be used to distinguish economic from noneconomic gas accumulations, resulting in significant exploration losses.

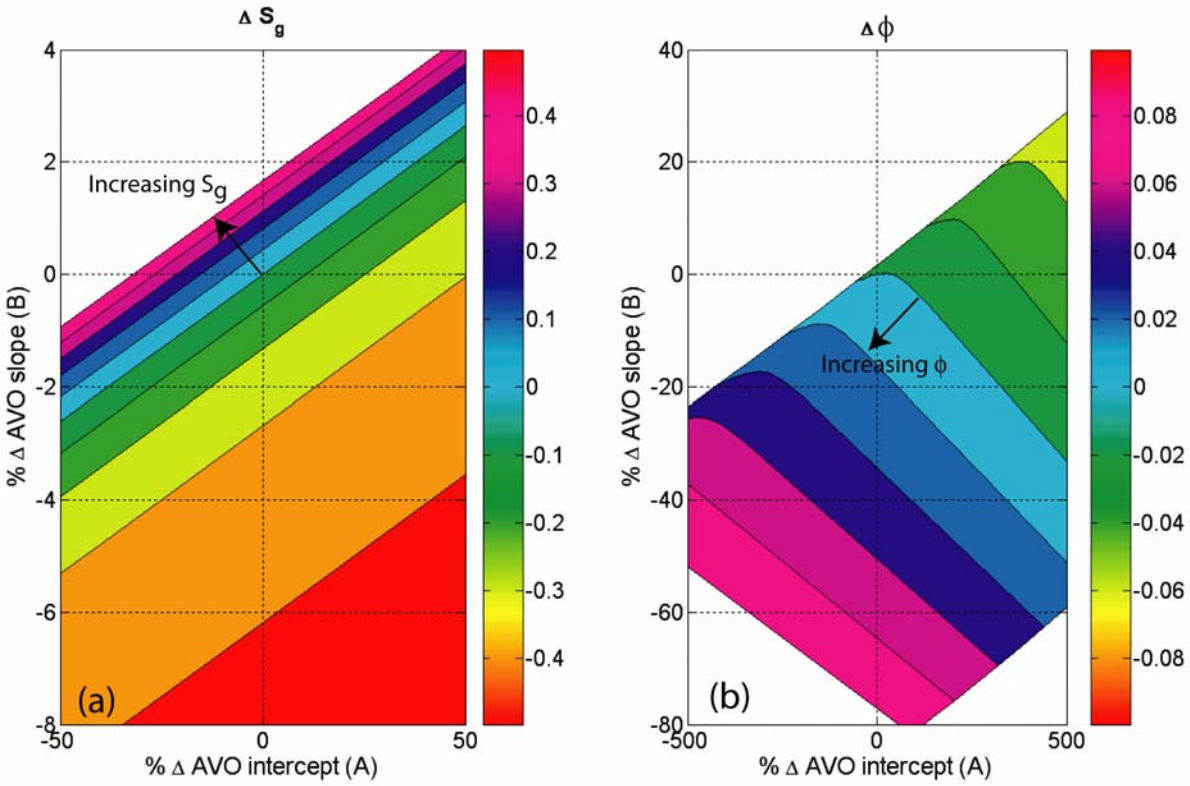

Figure 1. Reference point for calculations is porosity (ϕ) = 0.2, Gas saturation (S_g) = 0.5., S_{oil} = 0. Panel a) color contours of ΔS_g as a function of %Δ AVO intercept (A) and %Δ AVO slope (B). Panel b) color contours of $\Delta\phi$ as a function of %ΔA and %ΔB. Note that the axes for ΔS_o are a factor of 10 smaller than for $\Delta\phi$.

A simple rock-property modeling exercise is illustrative of the relative sensitivity of AVO data to gas saturation and porosity of sand encased in shale. We use parameters for sand and shale from a log in the Troll Field, North Sea, to be discussed below. The rock properties model for unconsolidated sand described by Dvorkin and Nur (1996) is used for calculating the V_p, V_s, and density (ρ) as a function of S_g and porosity (ϕ), in a brine-gas system, at reservoir conditions. The AVO intercept (A) and slope (B) (Aki and Richards, 1980) are calculated from V_p, V_s, and ρ. To see the sensitivity of A and B to changes in S_g and ϕ, the change in (Δ) A and B are calculated for values of S_g and ϕ that increment above and below reference values of S_g=0.5 and

ϕ=0.2. Figure 1 presents maps of the change in S_g and ϕ. The contour intervals are 0.1 in S_g (over a range 0.0-1.0) and 0.02 in ϕ (over the range 0.1-0.3), so that each contour interval represents a 10% change. In Figure 1, the origin corresponds to the reference case (S_g=0.5, ϕ=0.2). Contour lines represent constant ϕ in the case of ΔS_g (Figure 1a) or constant S_g in the case of $\Delta\phi$ (Figure 1b). The calculations show that increasing S_g by 10% (from 0.5 to 0.6) would produce a 3.1% decrease in A and a 0.22% increase in B (Figure 1a). By contrast, increasing ϕ by 10% (from 0.2 to 0.22) produces a 158% decrease in A and an 8% decrease in B (Figure 1b). These calculations can be recast in terms of changes in V_p and V_s or in terms of changes in acoustic and shear impedance with the same relative importance of ϕ versus S_g. The conclusion is that differences in A-B, V_p-V_s or acoustic-shear impedance produced by differences in S_g (excluding S_g values in the range of 0.0 to 0.1) are too small to be accurately estimated, given realistic noise levels of seismic data. On the other hand, differences in A-B, V_p-V_s or acoustic-shear impedance produced by differences in ϕ are one to two orders of magnitude larger than those produced by S_g, and should estimable from high-quality seismic data.

In contrast to the insensitivity of seismic attributes such as V_p-V_s, AVO slope and intercept or acoustic-shear impedance to gas saturation, the electrical resistivity of reservoir rocks is highly sensitive to S_g, through the link to water saturation. This sensitivity can be seen using Archie's law (Archie, 1942), which has been demonstrated to accurately describe the electrical resistivity of sedimentary rocks. Figure 2 shows the bulk resistivity (R_{bulk}) as a function of S_g=(1–S_w) for a sand having 25% porosity and brine salinity of 0.07 ppm at 60^0C (R_w= 0.05 Ω-m). The relationship between R_{bulk} and S_g has the advantage of the steepest slope in R_{bulk} occurring in the S_g range from 0.5 to 1.0, where the division between economic and noneconomic S_g usually occurs.

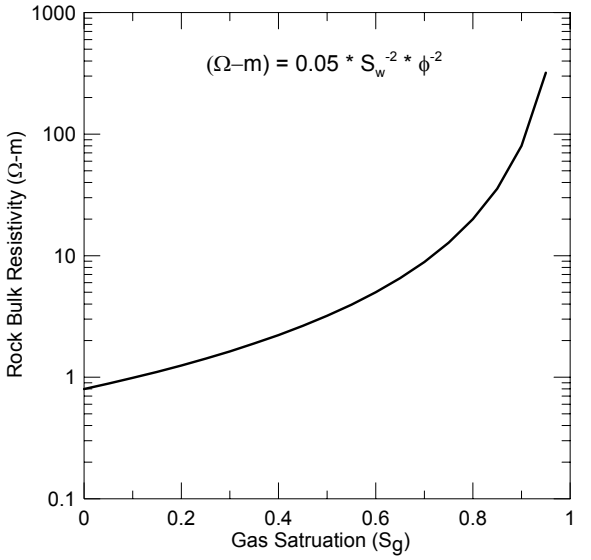

Figure 2. Rock bulk resistivity calculated from Archie's Law. R_w=0.05 for 0.07 Salinity @ 60C.

The means of providing estimates for R_{bulk} have recently become available through the use of controlled-source electromagnetic sounding systems. Developments over the last decade in the petroleum application of marine electromagnetic systems were driven, first, by the need for structural information in areas where high-velocity materials such as salt or basalt covered prospective sediments. Both CSEM and passive source magnetotelluric (MT) systems were considered for petroleum-related exploration (Hoversten and Unsworth, 1994). It was noted from the beginning that CSEM systems have superior resolving capabilities when compared to MT, but the logistics of deployment and ease of data interpretation favored MT, resulting in a preponderance of work on marine MT systems (Hoversten et al., 1998; Constable et al., 1998; Hoversten et al., 2000). The development of

CSEM systems actually predates the marine MT systems, in which CSEM was used for crustal investigations of the deep oceans (Filloux, 1983; Constable, 1990; Constable and Cox, 1996). In the last few years, attention has been focused on the use of CSEM systems in direct detection/mapping of hydrocarbons (Ellingsrud et al., 2002).

A marine CSEM system consists of a ship-towed electric dipole source and a number of seafloor deployed recording instruments capable of recording orthogonal electric fields. In the last few years, a number of contractors have begun offering marine CSEM data on a commercial basis. Marine CSEM data has the potential to enhance the prediction of reservoir parameters over that which can be done using industry-standard AVA techniques alone, because of its high sensitivity to water saturation. In this paper we illustrate the benefits of joint AVA-CSEM inversion for estimating fluid saturations and porosity from synthetic and field data.

Model Parameterization

There are substantial differences in the nature of energy propagation in the earth caused by a seismic source as opposed to a CSEM source. Of particular importance to the joint inversion of seismic AVA and marine CSEM data is the high attenuation of electromagnetic energy compared to that of seismic energy. After appropriate seismic processing (including amplitude recovery), we will assume that the seismic attenuation in the earth above the target interval (the overburden) have been accounted for and so can be neglected in the seismic modeling. However, this assumption cannot be made for modeling CSEM data, because the effects of the overburden on the target zone response are large and cannot be estimated independently, as is the case with velocity analysis. This means that the CSEM calculations require a model with electrical conductivity described from the sea surface down (an infinite air layer is also included), while the seismic calculations only require reflection coefficients to be calculated over the area of interest.

Since the CSEM and AVA calculations require different model domains, we have chosen to parameterize the model as illustrated in Figure 3. Layers of variable thickness (layer thickness can be an inversion parameter) are common to all zones of the inversion domain. The electrical conductivity (σ) from the air-sea interfaced to the top of the reservoir interval are parameters. A zone above the reservoir interval is also parameterized by V_p, V_s, and density (ρ). The reservoir interval is parameterized by porosity (ϕ) and fluid saturations (S_w, S_g, S_o). Pore pressure

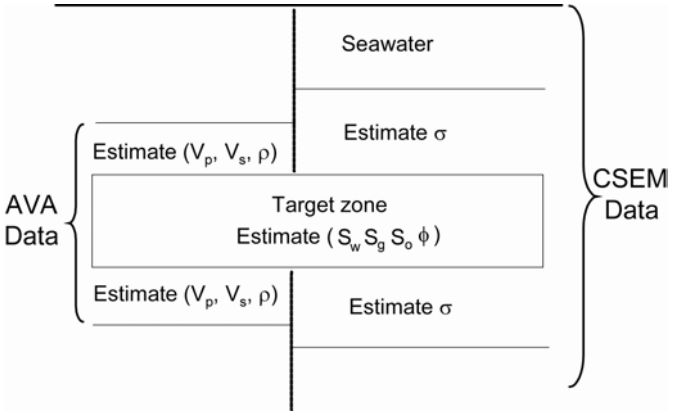

Figure 3: Inversion domain. Target zone is parameterized by S_w, S_g, S_o, and $\tilde{\phi}$. Target zone is surrounded by V_p, V_s and density zone for AVA data and surrounded by conductivity zone for CSEM data.

is also included in the algorithm, but will be assumed constant for the examples shown here. Below the reservoir, layers are again parameterized by σ, V_p, V_s, and ρ. Above the target zone, σ is required for the solution of the CSEM forward problem. Overburden V_p, V_s, and ρ above the target are required for two reasons. First, the time interval for the seismic data used in the inversion is chosen from a time-to-depth conversion based on the available velocity model, which may be in error. If the depth to the top of the target (reservoir) zone does not exactly tie to the selected time window, the inversion can adjust V_p above the target zone as a correction. Secondly, log information required to calculate the rock properties model is usually only taken within the reservoir, so that we can only describe the target zone itself in terms of fluid saturations and ϕ. However, we need properties for the layer directly above the reservoir to calculate the reflection coefficient at the top of the reservoir. The V_p, V_s, and ρ below the target interval are not strictly required, but provide continuity in the seismic data fit at times below the reservoir.

Inversion Algorithm

We have chosen to cast the inverse as a nonlinear least-squares problem, in which we minimize the Tikhonov functional (Tikhonov and Arsenin, 1977)

$$\theta = 1/2\left\{\left(F\left[m\right]-d^{obs}\right)\right\}^{T} D^{-1}\left\{\left(F\left[m\right]-d^{obs}\right)\right\}+\lambda/2\left(m^{T}W^{T}Wm\right) \qquad (1)$$

where T denotes transpose. W is a regularization matrix (we use the first spatial derivatives of the model parameters) that does not depend on m, and $F[m]$ is the forward model to produce a calculated response to be matched to the observed data, d^{obs}. The data covariance matrix, D, has estimated data variances on the diagonal and zeros off the diagonal. This is a common approach in geophysical inverse problems. Buland et al. (1996) applied Levenberg-Marquardt damped least-squares to AVO inversion of data from the Troll Field, where their algorithm uses the identity matrix rather than $\left(m^{T}W^{T}Wm\right)$ in Equation (1).

This approach is often referred to as a local (Tarantola, 1987) optimization as opposed to a global optimization (Xie et al., 2000). While a global approach is preferable for problems where the computational costs of the forward problems are low, they become impractical when the forward calculations become time- and/or memory-intensive. How much time and memory is considered too much increases each year with the advance of computer technology, but in general, any multidimensional geophysical forward problems involving wave propagation still are "too much" for most global inverse applications. The work reported on in this paper represents the first steps in a larger program to develop 3D joint seismic-CSEM inversion, and as such the algorithms are to be applied to 3D forward problems in the future.

One dimensional seismic AVA modeling uses the Zoeppritz equation (Aki and Richards, 1980) to calculate the angle dependent reflectivity, which is convolved with an angle-dependent

wavelet to form the calculated seismic data. The CSEM calculations are an integral equation solution for the electric (E) field from an electric dipole source located within a layered media (Ward and Hohmann, 1987). These forward models provide the derivatives of data with respect to the geophysical parameters (V_p, V_s, ρ and σ) that form the Jacobian (J) of normal geophysical inverse problems. The chain rule for derivatives is used to calculate the derivatives of the object function to be minimized (θ) with respect to the reservoir parameters. Equation (2) shows the derivative of θ with respect to S_g in terms of all the required partial derivatives.

$$\frac{\partial \theta}{\partial S_g} = \frac{\partial \theta}{\partial \sigma} \cdot \frac{\partial \sigma}{\partial S_g} + \frac{\partial \theta}{\partial V_p} \cdot \frac{\partial V_p}{\partial S_g} + \frac{\partial \theta}{\partial V_s} \cdot \frac{\partial V_s}{\partial S_g} + \frac{\partial \theta}{\partial \rho} \cdot \frac{\partial \rho}{\partial S_g} \tag{2}$$

The first half of each term on the right of Equation (2) comes from the geophysics, and the second half from the rock-properties model.

The partial derivatives relating changes in geophysical data with respect to changes in model parameters are calculated by finite-differencing of forward solutions about the current model for fast 1D problems, and by the adjoint method for the CSEM portion of the problem using finite difference methods (Newman and Hoversten, 2000) for 3D problems. The model parameters can be any reservoir parameter (i.e., water saturation, oil saturation, gas saturation, porosity, and pore pressure). In the examples presented in this paper, fluid saturations and porosity are considered as inversion parameters, with pore pressure held constant.

Linearizing (1) about a given model, m^i, at the i^{th} iteration produces the quadratic form;

$$\left[J^T S^T S J + \lambda W^T W + \alpha C^T C \right] m_{i+1} = J^T S^T S J m_i + J^T S^T S \delta d_i + \alpha C^T h \tag{3}$$

where m_{i+1} is solved for using a quadratic programming algorithm (Fletcher and Jackson 1974) that allows for upper and lower bounds on the parameters. S is a matrix containing the reciprocals of the data standard deviations such that $S^2 = D^{-1}$. The current difference between calculated (d_i) and observed data (d^{obs}) is given by $\delta d_i = d^{obs} - d_i$. The Lagrange multiplier (trade-off parameter) λ is adjusted from large to small as iterations proceed. That the fluid saturations sum to unity can be imposed as an additional constraining equation, $Cm_i = h$, where 1's in the rows of C multiply the saturations in m_{i+1}, and the elements of h corresponding to sums of saturations equal 1. Elements of h that correspond to porosity are 0. The α is fixed at a value (100 in these examples) large enough to insure $Cm_i = h$ to within a very small tolerance. When variable layer thicknesses are added to the parameter vector, an additional row is added at the bottom of C with 1's at positions corresponding to layer thickness in the parameter vector, and an additional value equal to the desired total thickness of the variable layers is added to the

end of *h*. This addition provides the further constraint that the inversion interval has the total thickness of the reservoir interval.

The parameter covariance of m is:

$$Cov(m) = M^{-1} J^T S^T S J M^{-1} \tag{4}$$

where

$$M = \left[J^T S^T S J + \lambda W^T W + \alpha C^T C \right]. \tag{5}$$

There are many approaches for setting λ in the inversion. Constable et al. (1987) use a golden section search for determining λ, which requires on the order of ten additional forward problem calculations per iteration, in addition to those required for calculation of the Jacobian. This approach is robust, but the run time requirements are impractical for full 3D CSEM inversion. Instead, we have adopted a simpler approach described by Newman and Alumbaugh (1997), one that has been demonstrated to be effective for large-scale CSEM problems. In this scheme, λ is selected as the iteration weighted maximum row sum of the matrix product $\left[J^T S^T S J \right]$, where

$$\lambda = \underset{1 \le m \le np}{Max} \left| \sum_{j=1}^{np} a_{mj} \right| / 2^{(i-1)} \quad . \tag{6}$$

Here a_{mj} is an element of $\left[J^T S^T S J \right]$, *np* is the number of parameters, and *i* is the inversion iteration number.

Rock-Properties Model

Direct inversion for the reservoir parameters requires a rock-properties model that links the reservoir and geophysical parameters. The model we have adopted uses the Hertz-Mindlin (Mindlin, 1949) contact theory for the dry frame bulk (K_{dry}) and shear (G_{dry}) moduli of a dense, random pack of spherical grains. Modified Hashin-Shtrikman lower bounds (Hashin and Shtrikman, 1963) are used to calculate the effective moduli for porosities below the critical porosity. This model is described by Dvorkin and Nur (1996) as applied to modeling velocity-pressure relations for North Sea Sand stones, and its use in combined seismic and EM inversion is described by Hoversten et al. (2003). Archie's law (Archie, 1942) is used to model electrical resistivity as a function of ϕ and S_w. The fluid bulk moduli (K_{brine}, K_{oil}, K_g) and densities ($\rho_{brine}, \rho_{oil}, \rho_g$) of brine, oil, and gas respectively are computed using relations from Batzle and Wang (1992).

The field data examples presented in this paper come from the Troll Field in the North Sea. Seismic rock-properties model parameters are found by using a simplex algorithm to minimize L_1, given by Equation (7).

$$L_1 = \sum_1^N \left| V_p^{obs} - V_p^{calc} \right| + \sum_1^N \left| \rho^{obs} - \rho^{calc} \right|, \tag{7}$$

where $V_p^{obs}, V_p^{calc}, \rho^{obs}, and\, \rho^{calc}$ are the sonic log compressional velocity, model-calculated compressional velocity, log density, and model calculated density, respectively. The units used in defining L_1 are m/s and Kg/m^3, so that the velocity and density have approximately equal numerical magnitude and hence equal weight in the value of L_1. If shear-velocity logs are available, V_s data misfit can be added to L_1. Log data from a well approximately 4 km to the northeast of the site used for the inversion tests (to be discussed below) was used to derive the rock-properties model. Figure 4 shows the log data with the calculated fit over the reservoir interval. Table 1 shows the parameters fixed in the inversion (assumed known) and those determined by the regression. The values for the Shear modulus, grain Poisson ratio, and grain density are very close to that of feldspar. For the inversions of Troll Field data, the parameters shown in Table 1 were used.

Table 1. Fixed Parameters for rock-properties model regression and parameters determined from the regression.

Fixed Parameters	
Critical Porosity	0.38
Oil API	28.5
Brine Salinity	0.07
Gas Gravity	0.59
Temperature (C)	65

Regression Fit	
Grain Shear Mod.	22.5
Grain Poisson	0.34
Grain Density	2567
# Contacts/grain	13.5

The three parameters, *C*, *m* and *n*, of Archie's law, Equation (8), are found by linear regression in the log10 domain:

$$R_{bulk} = CS_w^{-m}\phi^{-n} \tag{8}$$

Employing the S_w, R_{bulk}, and ϕ logs from the same well used for the seismic model parameters yielded values of 0.78 Ω-m, 1.31 and 0.14 for *C*, *m*, and *n*, respectively. The low value of *n* indicates very little sensitivity to porosity. This was also noted in developing Archie's law parameters for logs from the Snorre field in the North Sea (Hoversten et al., 2001) and was caused, in that case, by clay filling the pore space. The effects of the small value of n on the inversion for porosity will be discussed further below.

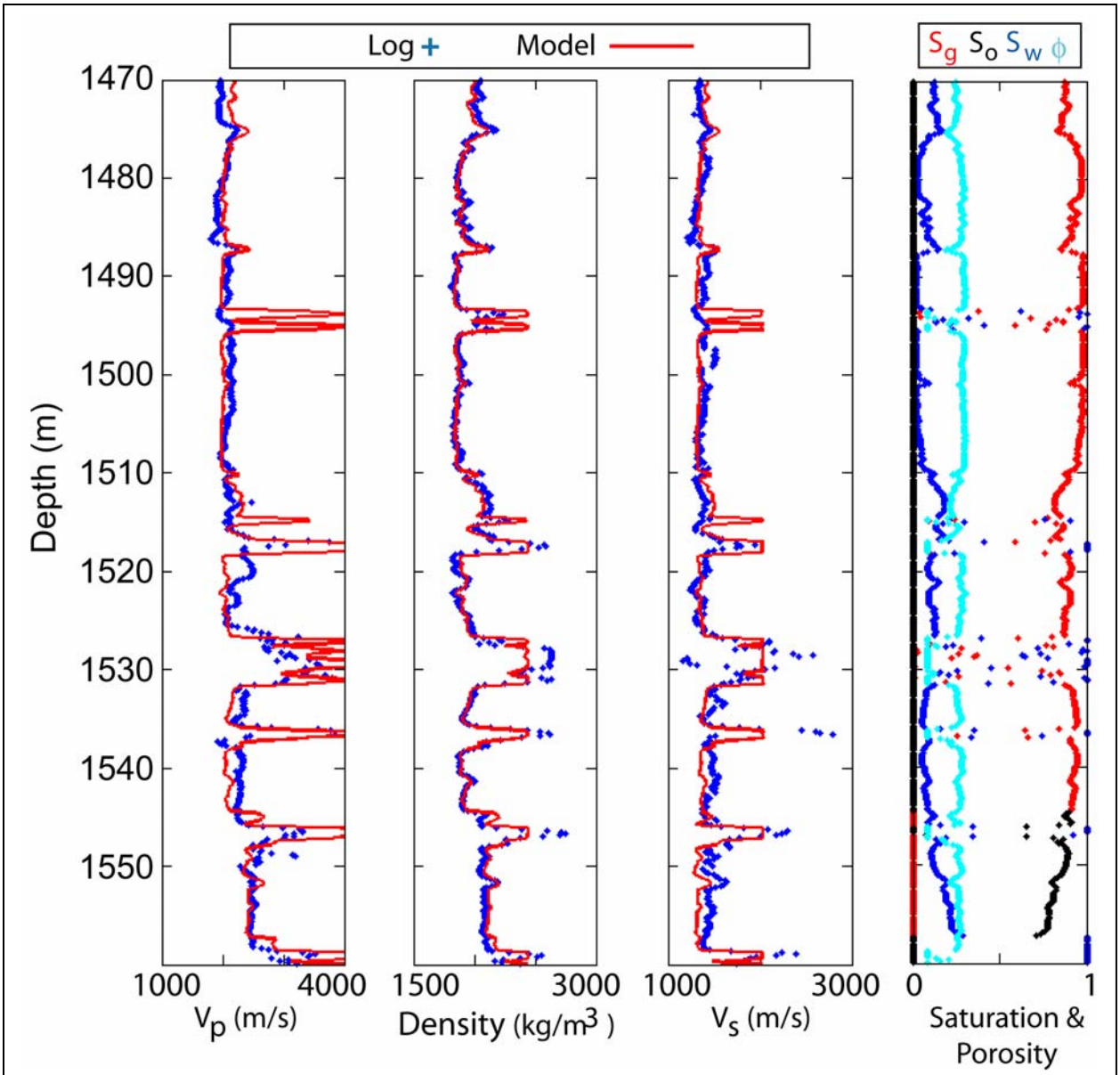

Figure 4. Rock-properties regression fits for data from a well 4 km to the northeast of the site where AVA and CSEM data are jointly inverted. Log V_p, density and V_s (blue crosses) compared to calculated values (red line) from regression fit are shown in the left most three panels. Input saturations and porosity are shown in right panel.

Synthetic Example

To illustrate the properties of the individual and combined inversion of AVA and CSEM data, we have constructed a simple five-layer model, from the rock-properties parameters given in Table 1 and the Archie's law parameters given above. The synthetic AVA data is sampled at 2 ms for seven angles (7.2, 13.5, 19.7, 25.6, 31.1, 36.3, and 41.0 degrees). Gaussian random noise

was added, starting with a signal-to-noise ratio (SNR) of 5 for the first angle and decreasing to a SNR of 2.5 for the far angle. The CSEM data is the amplitude and phase of the electric field at 3 frequencies (0.25, 0.75, 1.25 Hz) for 8 source-receiver offsets (0.775, 1.7, 2.5, 3.3, 4.1, 4.5, 5.7, and 6.5 km) from an electric dipole source 50 m off the seafloor and electric field receivers on the seafloor. Twenty percent Gaussian noise was added to the electric fields at the near offsets, increasing to 40 % at the maximum offset. The model has 1 km of seawater, with the target zone 1.4 km below the sea floor. Overburden (between seafloor and top of the target zone) conductivity is 1 Ω-m. The target zone is comprised of five 25 m thick layers, each with variable ϕ and S_g, with $S_o = 0$.

We tested two starting models: (1) all five layers with constant $S_g = 0.5$, $\phi = 0.2$ within the target zone, and (2) S_g = (0.7, 0.2, 0.7, 0.2, 0.7), ϕ = (0.2, 0.2 ,0.2, 0.2, 0.2) for the five layers from top to bottom within the target zone. AVA-only, CSEM-only, and joint AVA-CSEM inversions are presented to illustrate the sensitivities of the data used separately and together. The target RMS misfit of the error-weighted data was 1.0 and was reached in all inversions unless otherwise stated.

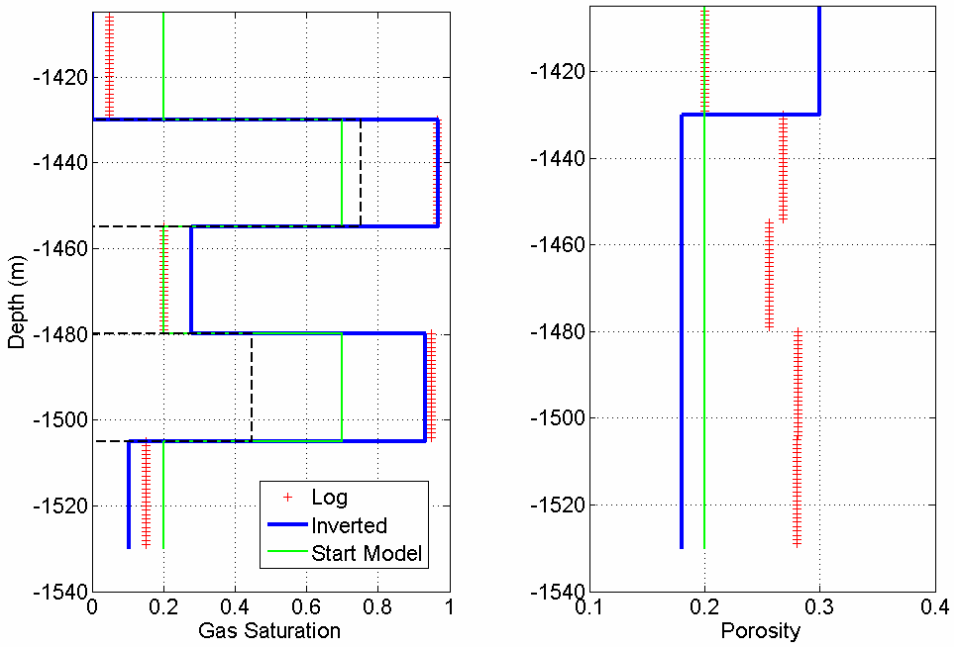

Figure 5. CSEM-only inversion of synthetic model target zone. True values are + symbols. Starting values (green line), from top to bottom layer were S_g = (0.2, 0.7, 0.2, 0.7, 0.2), ϕ = (0.2, 0.2, 0.2, 0.2, 0.2). Blue lines show final parameter estimates from inversion. Black dashed lines represent +- 1 standard deviation of model parameters.

Both CSEM-only and AVA-only inversions that began with uniform Sg=0.5 failed to converge to a model anywhere near the true model. Both inversions became trapped in local minimum in the object function, far from the true model. In order for either CSEM-only or

AVA-only inversions to converge to a nearly correct model they had to be started from S_g = (0.7, 0.2, 0.7, 0.2, 0.7), ϕ = (0.2, 0.2 ,0.2, 0.2, 0.2). This starting model, with layers 2 and 4 having higher S_g than the surrounding layers, produces individual inversions (CSEM -only and AVA-only) that distinguish the two high S_g layers. Figure 5 shows the results of using the CSEM data only; Figure 6 shows the results of using only AVA data. Using only the CSEM data produces S_g estimates that are very close in the high S_g layers and no more than 0.08 off in the low S_g layers. However the S_g standard deviations are large and only plot on the scale of the figure for the high S_g layers. The CSEM-only inversion provides essentially no information about the porosity.

The inversion of the AVA data produces better estimates of S_g in the top and bottom layers (low S_g), with much lower parameter standard deviations overall. The S_g estimate of the second high S_g layer is less accurate than that of the CSEM inversion. The seismic inversion has produced much better estimates of layer porosities when compared to the CSEM inversion.

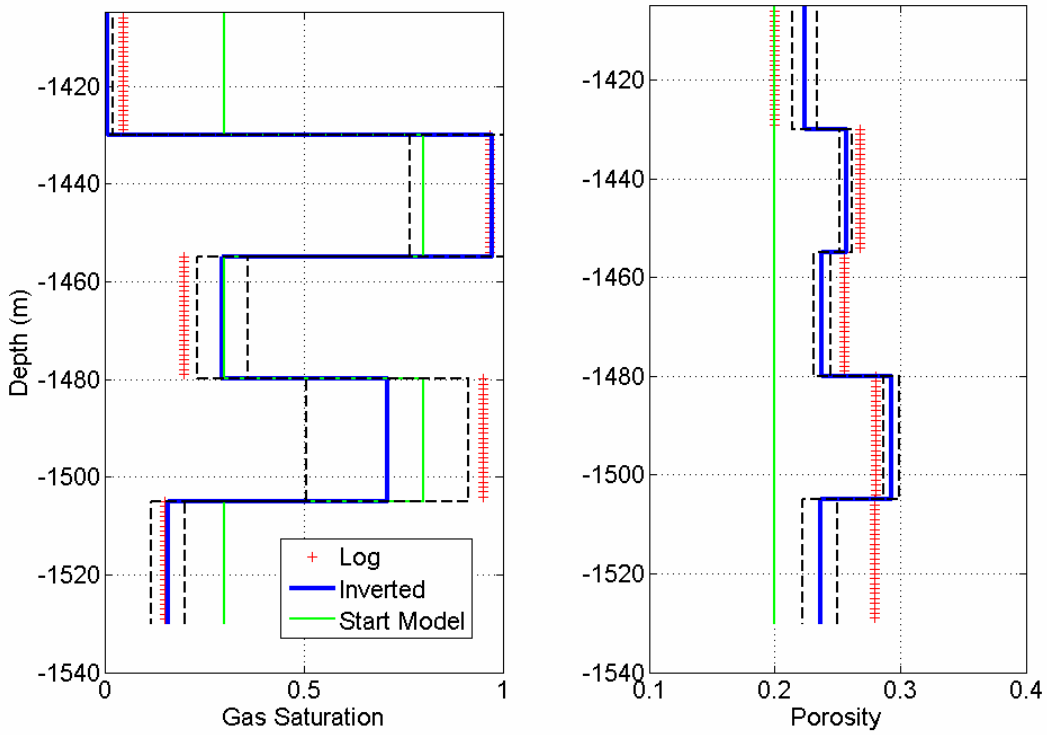

Figure 6. Inversion for gas saturation (left panel) and porosity (right panel) of synthetic model target zone, using only seismic AVA data. True values are + symbols. Starting values (green line), from top to bottom layer were S_g= (0.2, 0.7, 0.2, 0.7, 0.2), ϕ = (0.2, 0.2, 0.2, 0.2, 0.2). Blue lines show final parameter estimates from inversion. Black dashed lines represent +- 1 standard deviation of model parameters.

For the joint inversion of both the CSEM and AVA data, each data is weighted only by its assigned data errors. No relative weighting between CSEM and AVA data in Equation (2) was used, although this may be considered in certain circumstances if there is reason to believe that one data set should dominate (e.g., the CSEM data is thought to be highly 3D, so that the 1D assumption is less valid for the CSEM than for the seismic).

Figure 7 shows the S_g and ϕ estimates from jointly inverting both the CSEM and AVA data sets. The CSEM and AVA observed and calculated data from the inversion are shown in

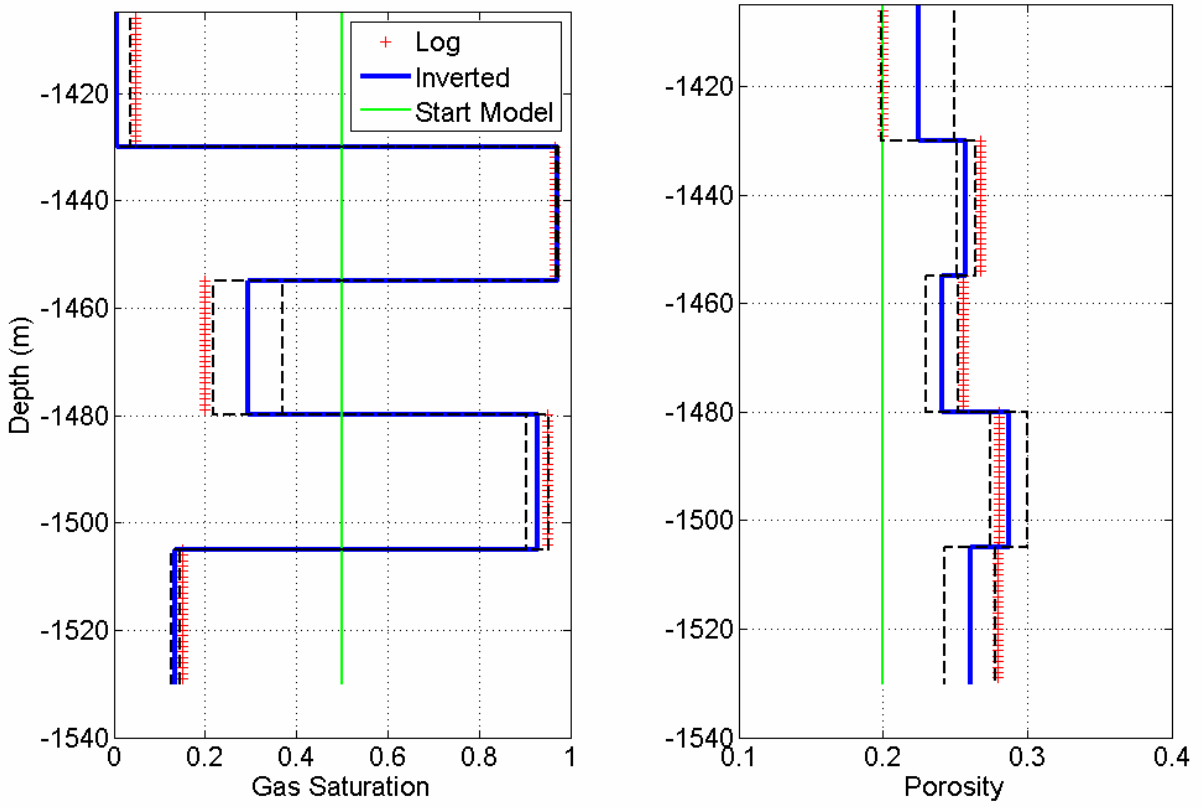

Figure 7. Inversion for gas saturation (left panel) and porosity (right panel) of synthetic model target zone, using seismic AVA and CSEM data. True values are + symbols. Starting values (green line), from top to bottom layer were S_g = (0.2, 0.7, 0.2, 0.7, 0.2), ϕ = (0.2, 0.2, 0.2, 0.2, 0.2). Blue lines show final parameter estimates from inversion. Black dashed lines represent +- 1 standard deviation of model parameters.

Figures9 and 10 respectively. The starting model here is the constant S_g and ϕ that caused both the CSEM and AVA inversions to find local minima that were not close to the true model. Here, the CSEM data has provided enough low wave number information so that when the seismic data is added, the joint inversion does not get trapped in local minima and produces a final model close to the true model. In general, the estimated S_g and ϕ are closer to the true values in the

joint inversion when compared to either the AVA- or CSEM-only inversions. The S_g estimates from the joint inversion are the same or better than those from the AVA-only inversion. In particular, the S_g estimates of the lower two layers are significantly closer to their true values in the joint inverse model (Figure 7) when compared to the AVA-only inverse model (Figure 6). In addition, the parameter standard deviations of the S_g estimates are decreased. The parameter standard deviations of the ϕ estimates are slightly increased in the joint inverse estimates when compared to the seismic only standard deviations. However, ϕ estimates for the first three layers are the same for the joint and AVA-only inversion, and the ϕ estimates of the lower two layers are improved in the joint inversion.

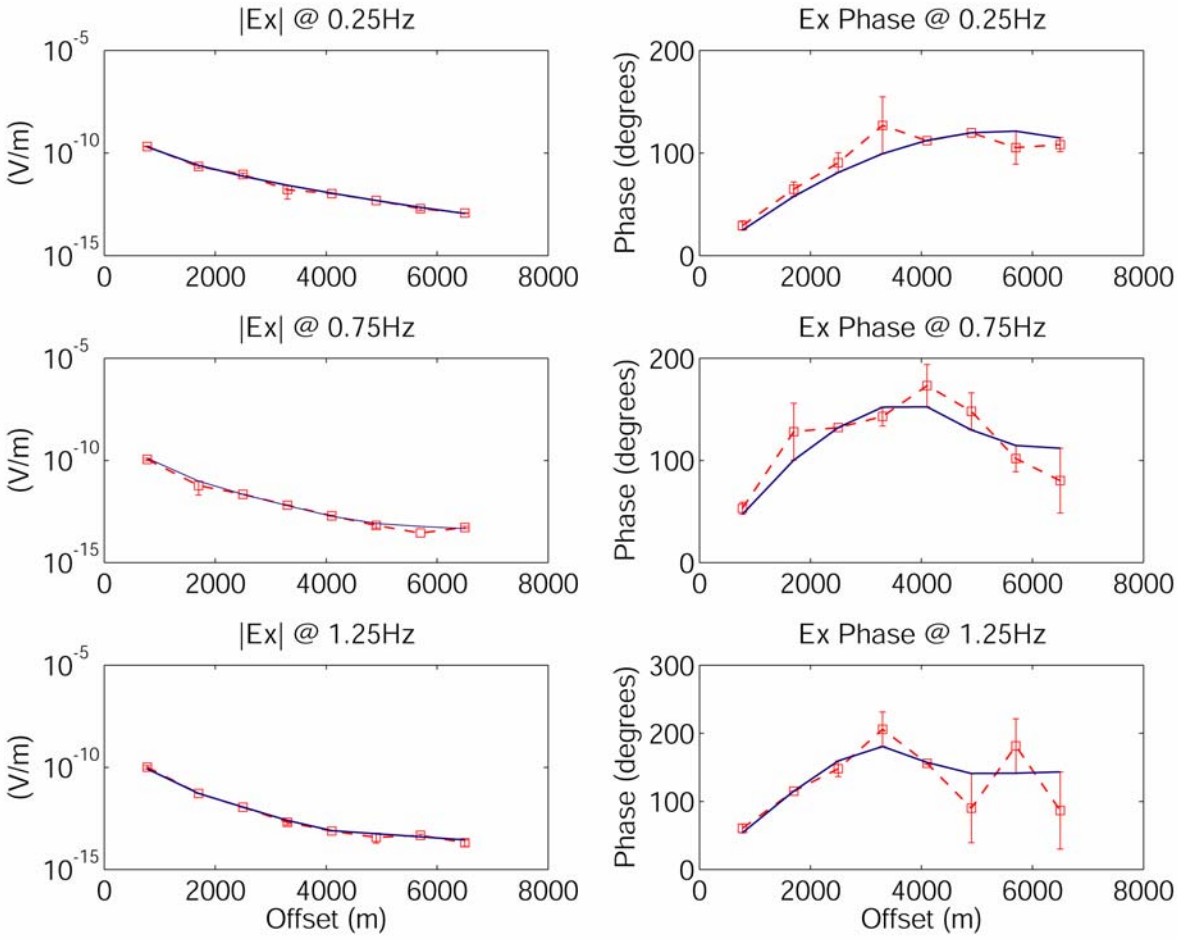

Figure 8. Synthetic marine CSEM data (red dashed curves with error bars) from the true model and calculated data (solid blue curves) from the joint inversion of synthetic AVA and CSEM data to produce the inverse model shown in Figure 7. The left panels are amplitude of the received electric field and the right panels are the phase of the received electric field.

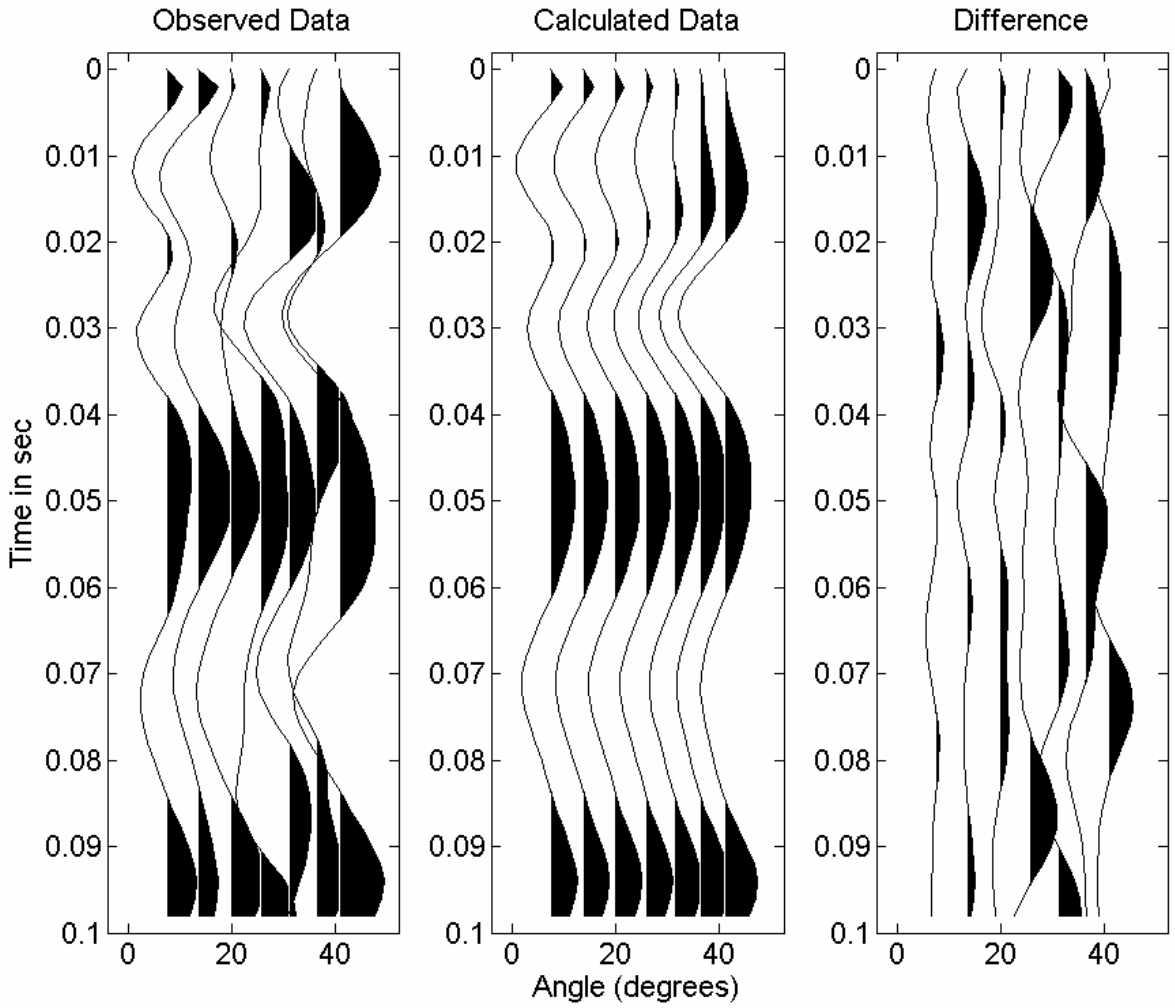

Figure 9. Observed, calculated and difference AVA data for joint inversion model shown in Figure 7. Left panel, synthetic data (considered as observed data by inversion) with SNR = 5 to 2.5 from near to far angle respectively. Middle panel calculated data from joint inverse model shown in Figure 7. Right panel, difference between observed and calculated data.

Sensitivity to Rock-Properties Model Parameters

For S_g and ϕ, the inversion of either the CSEM or seismic data in isolation or in combination relies on the parameters of the rock-properties model, which can be determined by laboratory core measurements and/or regression fits to log data as described above and in Hoversten et al. (2003). To check the sensitivity of the inversion to errors in the rock-properties model, the joint inverse shown in Figure 7 was run successively with 5% errors in each of the rock-properties parameters, and the mean error on ϕ and S_g was calculated (Figure 10). The red line in Figure 10 shows the mean errors in the S_g and ϕ estimates with exact rock-properties parameters. The parameters that control K_{dry} (grain density, grain shear modulus, critical porosity, number of

grain contacts, and grain Poisson ratio) are the most important. The inverse estimates of ϕ are less sensitive to rock-properties errors than is S_g. The sensitivity to parameters controlling K_{dry}

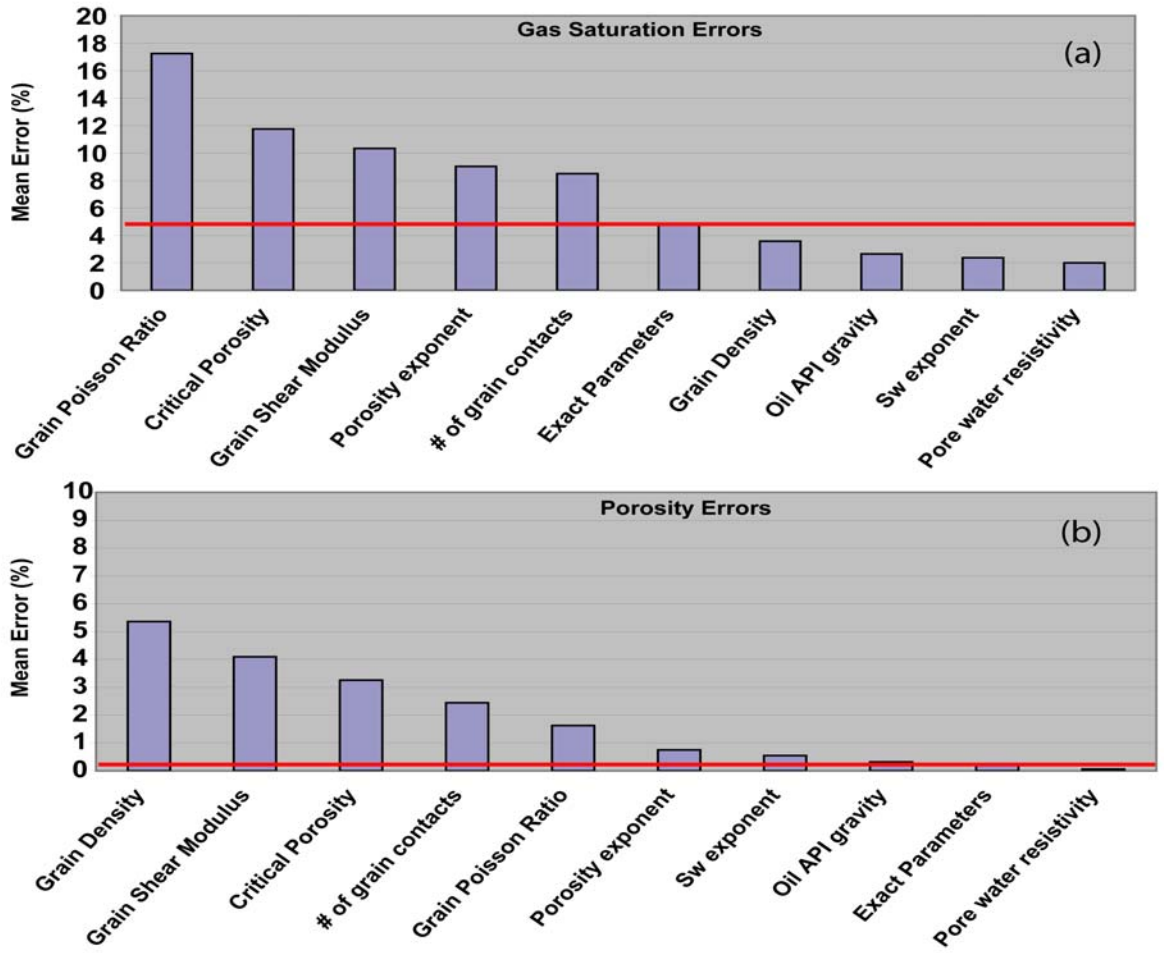

Figure 10. Mean absolute errors in inversion parameters for 5% error in rock properties parameters. Mean errors in S_g estimates are shown in panel (a). Mean errors in ϕ estimates are shown in panel (b).

can be understood by considering the Hertz-Mindlin representation of K_{dry};

$$K_{dry} = \left[\frac{l^2 \left(1-\phi_0\right)^2 G_{grain}{}^2}{18\pi^2 \left(1-\nu\right)^2} \cdot P_{eff} \right]^{1/3} \tag{9}$$

where ϕ_0 is the critical porosity (the porosity above which the grains become a liquid suspension), P_{eff} is the effective pressure, ν is the grain Poisson's ratio, G_{grain} is the grain shear modulus, and l is the average number of grain contacts per grain. Since K_{dry} is a non-linear function of ϕ_0, l, ν, G_{grain}, and P_{eff}, using K_{dry} directly would be preferred if core measurements of K_{dry} are available. When K_{dry} is used as a bulk parameter, not calculated from Equation (9), 5% errors on K_{dry} produce approximately 7% and 4% errors for estimated S_g and ϕ respectively.

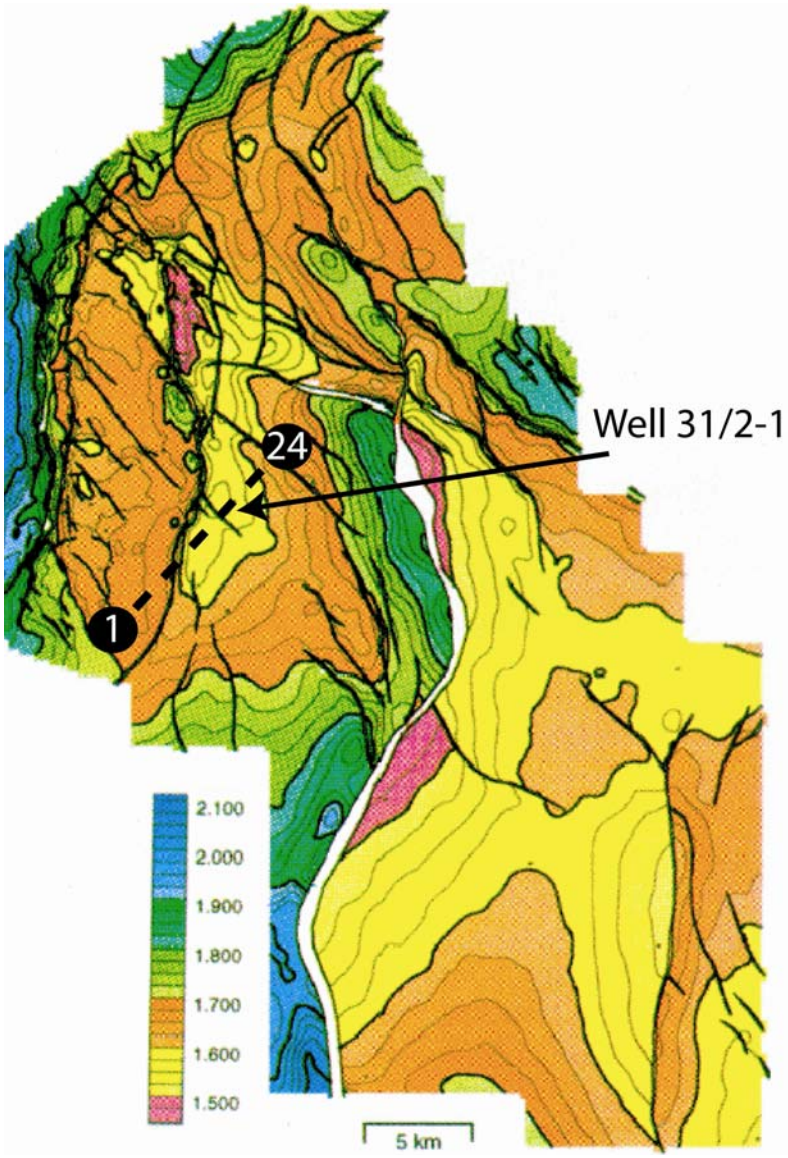

Figure 11. Troll top reservoir (Sognefjord) two-way time in seconds (after Hwang and McCorkindale, 1994). Marine CSEM line from Receivers 1 to 24. The location of the intersection of well 31/2-1 with the vertical plane containing the CSEM line is shown by the black arrow.

Troll Field Data

Seismic and marine CSEM data were acquired over a portion of the Troll Field in 2003. Figure 11 shows the location of the marine CSEM line (dashed line between receiver sites 1 and 24). Well 31/2-1 intersects the reservoir beneath the CSEM transect, as shown by the arrow in Figure 11. The CSEM receiver units were laid out in a line, with nominal separation of 750 m between location 1 and 24. A 200 m electric dipole transmitter, producing 200 amps, was towed at approximately 2 knots along the receiver line in both directions, producing data at the receivers for transmitters on either side of the receiver. The electric dipole transmitter is nominally aligned with the survey line, course corrections and ocean currents produce some variation in the orientation of the transmitter along the line. The received CSEM data along with

the transmitter locations and current are recorded as time series. In postprocessing, the CSEM time series are averaged to produce in-phase and out-of-phase electric field for average transmitter locations spaced 100 m apart along the line. The transmitter fundamental is 0.25 Hz. There is sufficient power to extract the third and fifth harmonics, so that three frequencies (0.25, 0.75, and 1.25 Hz) were acquired.

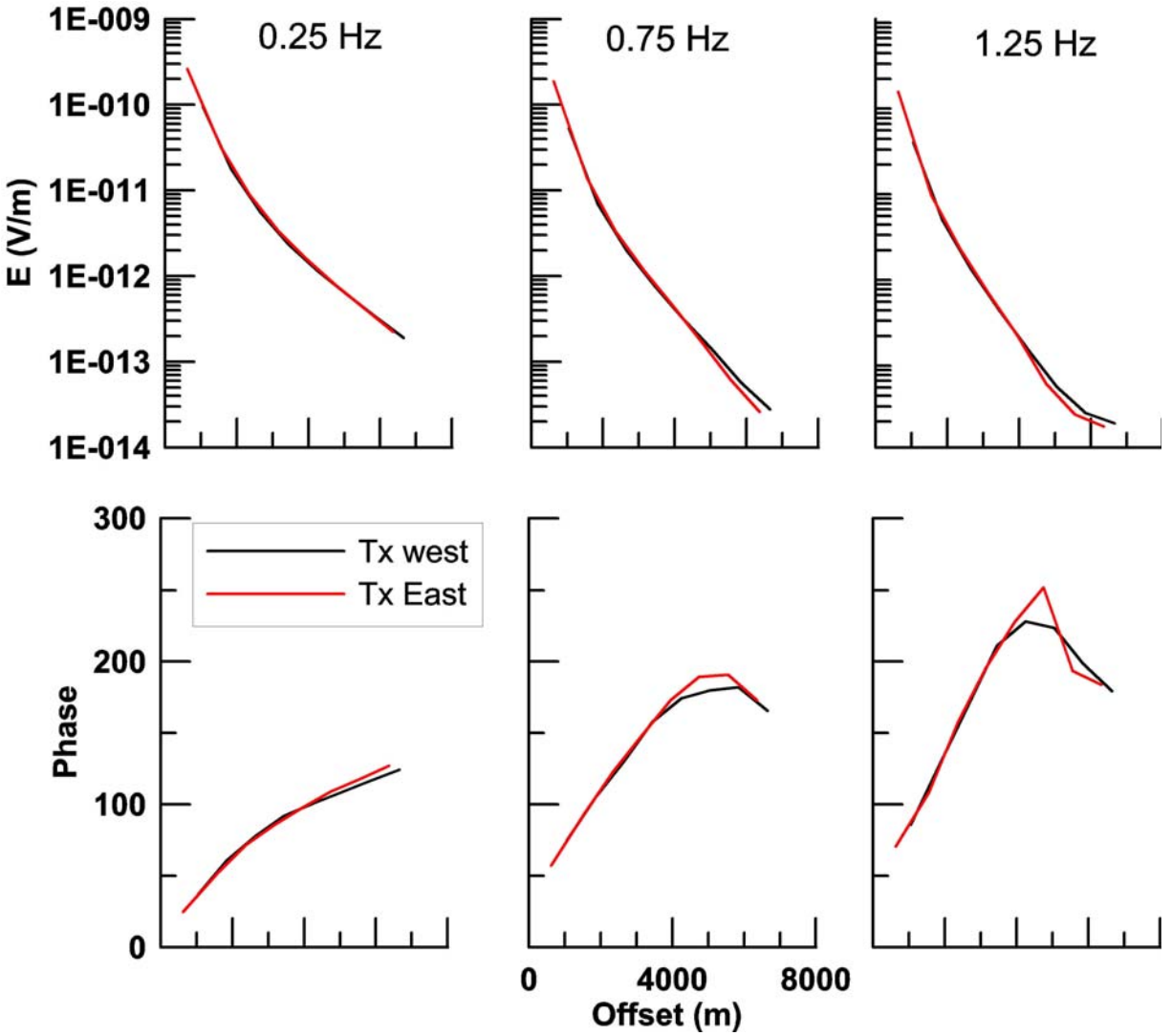

Figure 12. Electric field amplitude (upper row) and phase (lower row) at 0.25, 0.75, and 1.25 Hz as a function of the source-receiver offset (m) at a CSEM receiver near the 31/2-1 well. Transmitter locations to the west of the receiver are plotted in black, transmitter locations to th

Figure 12 shows the CSEM data converted to amplitude and phase of the electric field in the line direction (roughly parallel to the transmitter dipole orientation) from the receiver nearest the 31/2-1 well. If the earth had a one-dimensional conductivity structure (as the inversion forward

model assumes) the response, both amplitude and phase, would be identical for transmitters on either side of the receiver. We see that this is true for offsets up to about 4 km. Beyond 4 km, the difference between data from transmitters on either side of the receiver increases with offset and frequency. The largest asymmetry occurs for the highest frequency phase data at a 5 km offset.

In general, the spatial sensitivity of the CSEM data to this dipole-dipole configuration is a function of source-receiver offset, earth conductivity, and frequency, with lower frequencies and larger offsets having sensitivity to deeper changes (Spies, 1989). As the transmitter-receiver offset increases, the centroid of the sensitivity region moves downward and away from the receiver in the direction toward the transmitter. To approximate a 1D response, we have averaged the EM data for transmitters on either side of the receiver, thus causing the centroid of the sensitivity region of the averaged data to be directly below the receiver location.

The 3D seismic data was pre-stack time migrated and sorted into common-midpoint gathers. Normal move-out (NMO) and residual NMO was applied, along with multiple removal and filtering to a nominal zero-phase wavelet. The offsets were converted to angles by ray-tracing a layered model with velocity and density taken from the 31/2-1 well. Depth-time pairs were generated from the 31/2-1 well and used to determine the time window for the seismic data, such that the data covered the depth interval 100 m above and below the reservoir zone.

Ground Truth for comparrison and conditions of inverse models

No production has occurred in the area of the 31/2-1 well, where our data analysis takes place. The nearest production is from the oil rim (approximately 13 m thick) several kilometers from our site. It is expected that S_w has not changed by more than one or two percent since the logs were taken. The high gas saturation zone extends from 1415 m to 1544.5 m. There is a predominantly oil zone between 1544.5, the gas-oil contact (GOC), and 1557.5 m where original oil saturations were between 70 and 85%. Between 1557.5 m depth and the bottom of the logged interval, at 1670 m, is a paleo-oil-zone where original oil saturations were 20 to 30%. No gas or oil saturation logs are available, but time lapse seismic data has been interpreted as follows: Between the time of log measurements and the geophysical surveys used in this paper, production from the oil rim has lowered reservoir pressures enough that gas has been released from the oil in the oil- and paleo-oil-zones, resulting in a 5% increase in gas saturation in these zones. We therefore use the logged S_w to calculate oil and gas saturation as follows; above 1544.5m oil saturation (S_o) is assumed to be zero, and we assume $S_g = 1-S_w$, below 1544.5 m $S_o = 1-S_w-0.05$ and $S_g = 0.05$. The logged S_w and calculated S_g and S_o are used for comparing the performance of the different inversions. In addition to visual inspection of the results, we calculate three measures of agreement between the inversion predictions and the logs: (1) the RMS difference between inversion and log parameters, (2) the L1 norm of the differences between inversion and log parameters, and (3) the net, or integrated, value of the inverted and log parameters over the reservoir interval.

The starting model for all inversions of the Troll Field data have linear ramps in S_w and S_g such that S_w goes from zero to one and S_g goes from one to zero from the top to the base of the reservoir. The initial S_o is set to zero. The ϕ starting values came from blocking the ϕ log. The bounds used in the quadratic programming solver of Equation (3) were set at +- 0.3 for S_w and S_g (subject to a minimum and maximum of 0 and 1, respectively) and +- 0.1 for ϕ from their initial values. The upper bound on S_o is 0.1 above 1544.5 m where no oil was present in the original logs. Below 1544.5, the S_o upper bound begins at 0.7 at 1544.5 and decreases linearly to 0.1 at the base of the reservoir to allow oil where it was originally present. The lower bound on S_o is zero everywhere.

A sparse-spike acoustic impedance (AI) inversion (Levy and Fullagar, 1981) was first done on the zero-offset AVA trace. The layering from the acoustic impedance inversion was used to determine the minimum number of layers required in the reservoir interval. Initial inversions were begun with the layer thicknesses determined from the AI inversions in time and converted to depth using the log acoustic velocity. However, it was found that inversions starting with uniform layer thickness performed better than those starting with thicknesses derived from the AI time layers and assuming the log velocities, so the results shown in subsequent figures began with the number of layers determined from the AI inversion with a uniform 20 m thickness.

Because the inversions begin with a large value of λ used in Equation (1) (on the order of 1000 as determined by Equation (6)), the smoothing term dominates the initial iterations and produces the flattest model within the bounds on the first iteration. The starting models shown in Figure 13 are the input starting models before the first iteration. In subsequent inverse model plots for the AVA-only and joint AVA-CSEM inversions we show the model after the first iteration has smoothed the input model since this is effectively where the algorithm begins. The target data RMS misfit is 1.0. The target interval was divided into thirteen 20 m thick layers, with five seismic layers above and one seismic layer below the target zone. The conductivity overburden consisted of thirteen layers above the target zone. In addition to fluid saturations and ϕ in the target zone, layer thicknesses were added as inversion parameters in the AVA-only and joint AVA-CSEM inversions to accommodate placement of the sparse reflection coefficients.

CSEM-only inversion

The inversion for the CSEM data nearest the 31/2-1 well (Figure 12) is shown in Figure 13. The RMS data misfit achieved was 1.05. The CSEM data cannot distinguish between oil and gas since the electrical resistivity is only a function of S_w and ϕ, so only these parameters were used in the CSEM-only inversion. The observed and calculated CSEM data is shown in Figure 14. S_w at the top of the reservoir is 0.04, and then increases with depth. The inversion has decreased S_w from the starting model at the bottom of the reservoir and has smoothed out the blocked log porosity starting values to a mean porosity of 0.21 with higher porosity in the top 100 m of the reservoir. The inversion reflects the relative sensitivity of the bulk resistivity to S_w and ϕ, as discussed in the rock-properties section. The S_w standard deviations are small at the top of the reservoir (since the CSEM response is most sensitive to the presence of a resistor at the top of the

reservoir) and increase with depth, whereas the ϕ standard deviations are too large to plot on the scale of the figures (average standard deviation over the reservoir interval was 2.2). A very small Archie's law porosity exponent (low sensitivity to ϕ) translates to high variance in ϕ estimates.

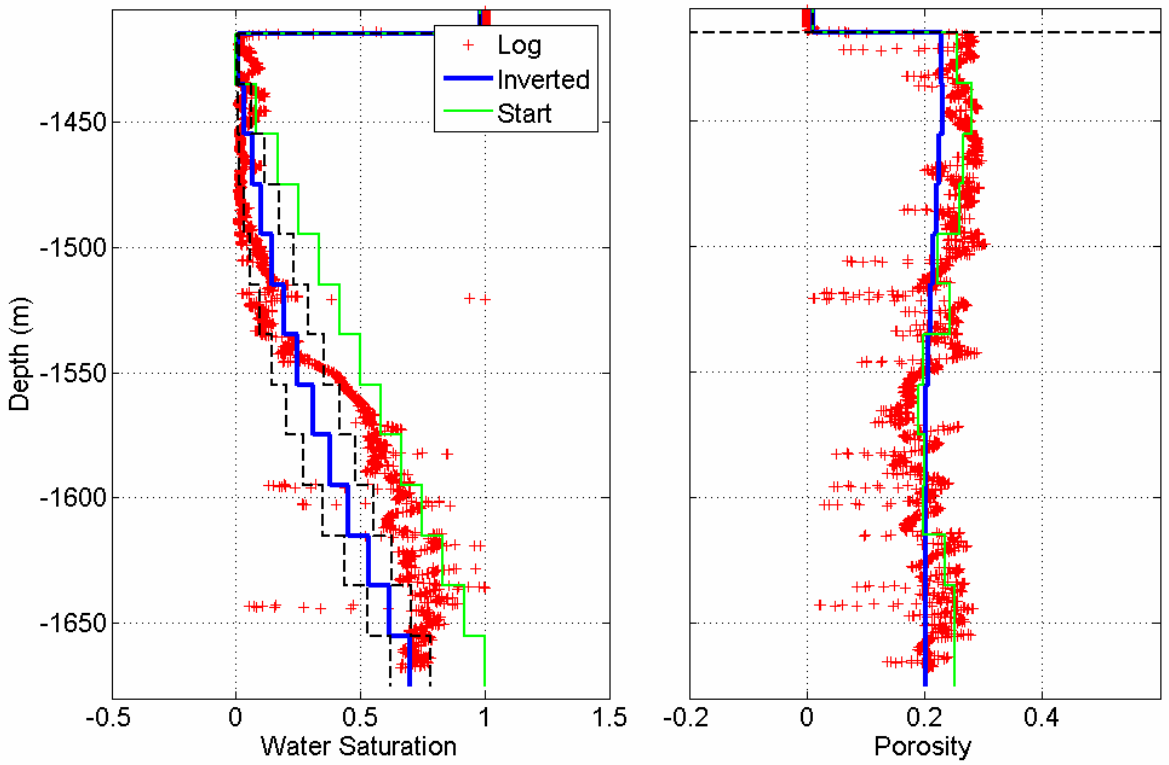

Figure 13. Inversion for S_w (left panel) and ϕ (right panel) using only CSEM data. Red plus signs are log values, the green line is the starting model, and the blue line is final inversion model. Black dashed lines are the 1 standard deviation bounds. Porosity bounds are too large to plot on the figure, with the average standard deviation equal to 2.2.

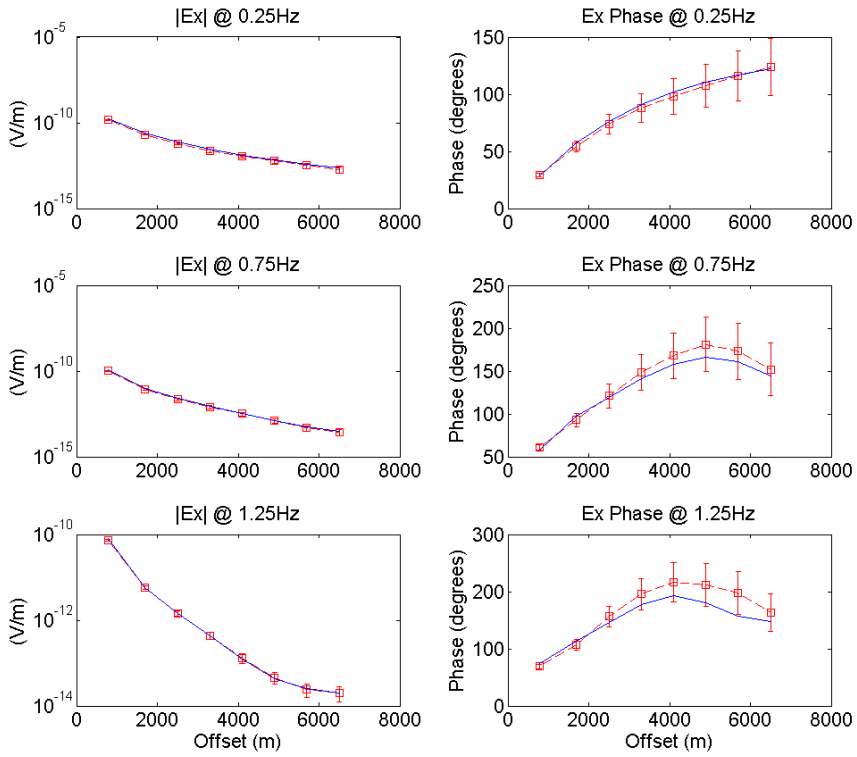

Figure 14. Observed and calculated inline E amplitude (left column) and phase (right column) for CSEM-only inversion model shown in Figure 13. The total RMS data misfit is 1.05.

AVA-only inversion

Inversions of AVA-only and combined AVA-CSEM data were parameterized by S_w, S_g, S_o, ϕ and layer thickness within the reservoir zone. Figure 15 shows the inverse model from inversion of the AVA-only data nearest the 31/2-1 well. The RMS data misfit achieved was 0.87. The inversion has decreased S_w and increased S_g in the upper 100 m of the reservoir. Porosity estimates are much closer to logged values than in the case of the CSEM-only inversion, with significantly smaller ϕ standard deviations compared to the CSEM-only inversion. All inversions that include AVA data produce ϕ estimates with low parameter standard deviations. This is consistent with the high sensitivity the AVA response to changes in porosity as shown in Figure 1. The inversion has estimated gas and water in the lower half of the reservoir rather than the oil that is present. The depths of the top of gas, the gas-oil contact, and the top of the paleo-oil-zone and the base of the logged interval are marked as T1, T2, T3, and T4 respectively at times that have been converted using the log velocity.

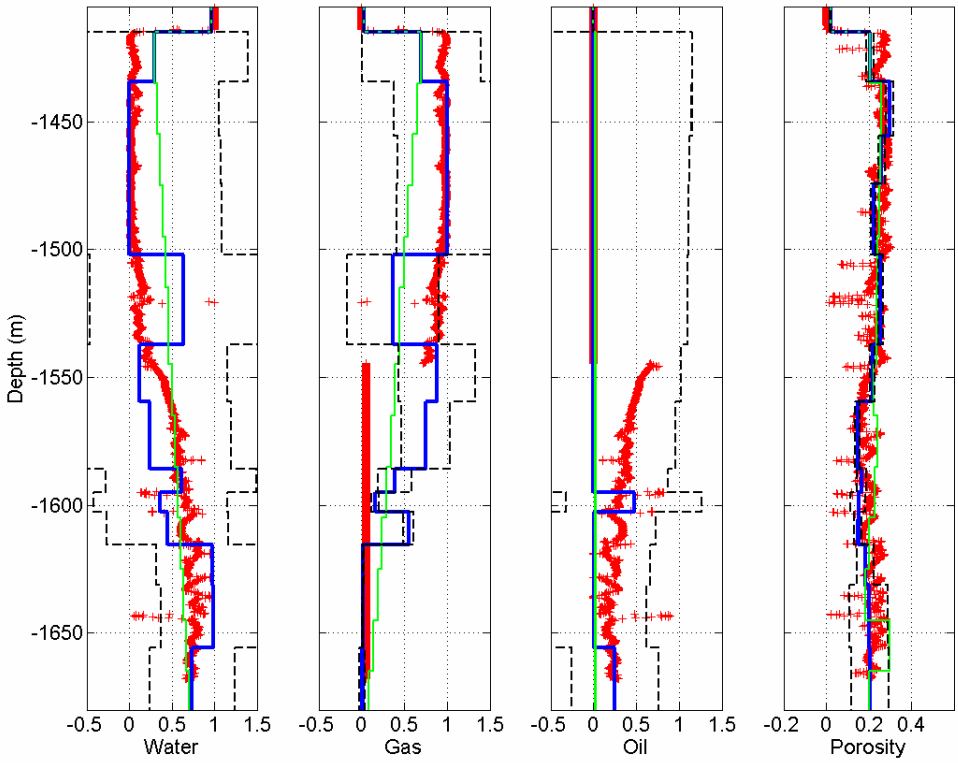

Figure 15. Inversion estimates of water (left panel), gas (second from left), oil (second from right) and porosity (right panel) using only seismic AVA data. Red plus signs are log values, green line is parameter values after first iteration (when smoothing has flattened the starting model), and the blue line is the final inversion model. Black dashed lines are one standard deviation of the model parameters.

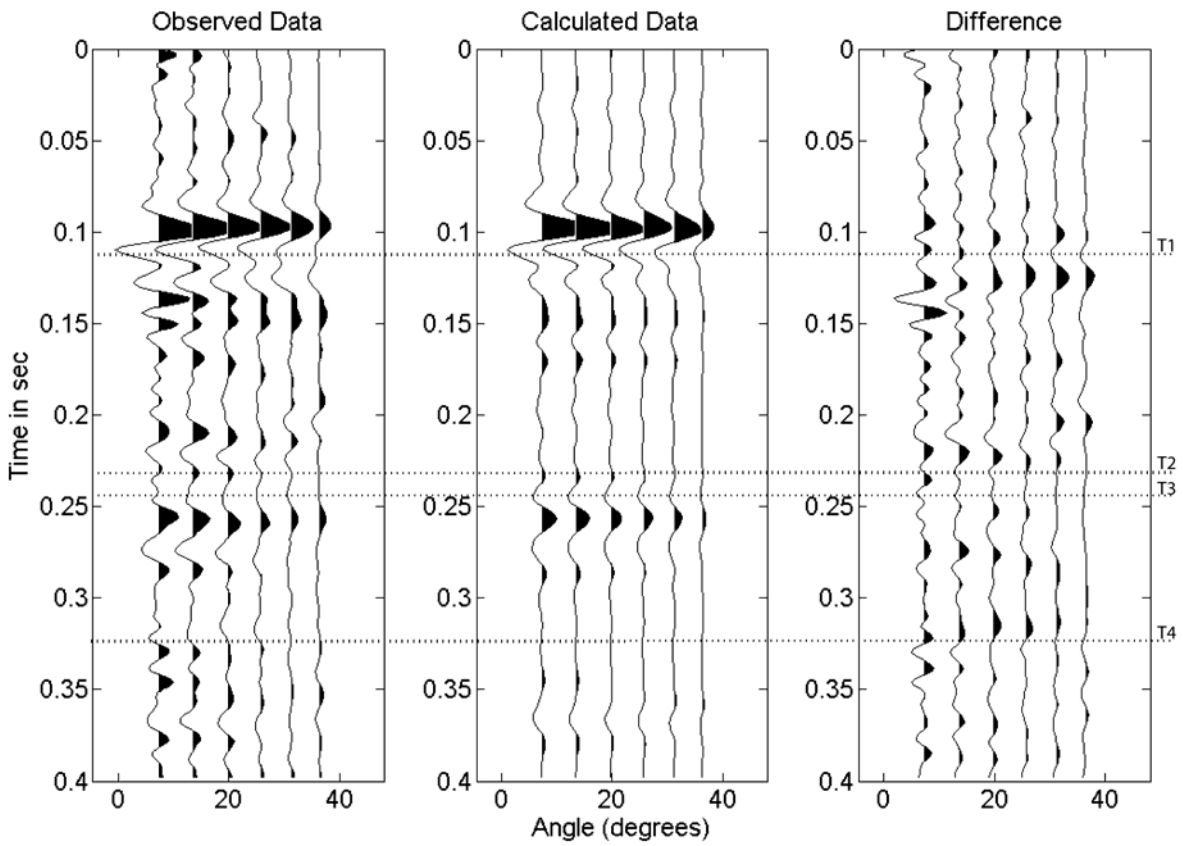

Figure 16. Observed seismic AVA gather (left panel), calculated AVA data from AVA-only inversion shown in Figure 15 (middle panel), and difference between observed and calculated AVA data (right panel). Zero time corresponds 1300 m depth. Times marked as T1, T2, T3, and T4 on right side of figure correspond to top of gas, gas-oil contact, top of paleo-oil zone and bottom of logged interval respectively. The RMS data misfit is 0.87.

AVA-CSEM inversion

Figure 17 shows the inversion of the CSEM and AVA data simultaneously. The combined RMS data misfit is 0.91. The joint inversion has decreased S_w and increased S_g in the top 100 m of the reservoir, much as the AVA-only inversion. However, the saturation estimates are much closer to the logged values in the lower half of the reservoir compared to the AVA-only inversion. Here, the S_g has been reduced to near zero from the starting model, and S_o has been added. The influence of the CSEM data has been to reduce the S_w in the lower half of the reservoir (as the CSEM-only inversion did), so that the S_w estimates from the joint inversion fall between those of the CSEM-only and the AVA-only estimates. The parameter standard deviations have been reduced for all parameters, most significantly for S_w and S_o compared to the AVA-only inversion results shown in Figure 15.

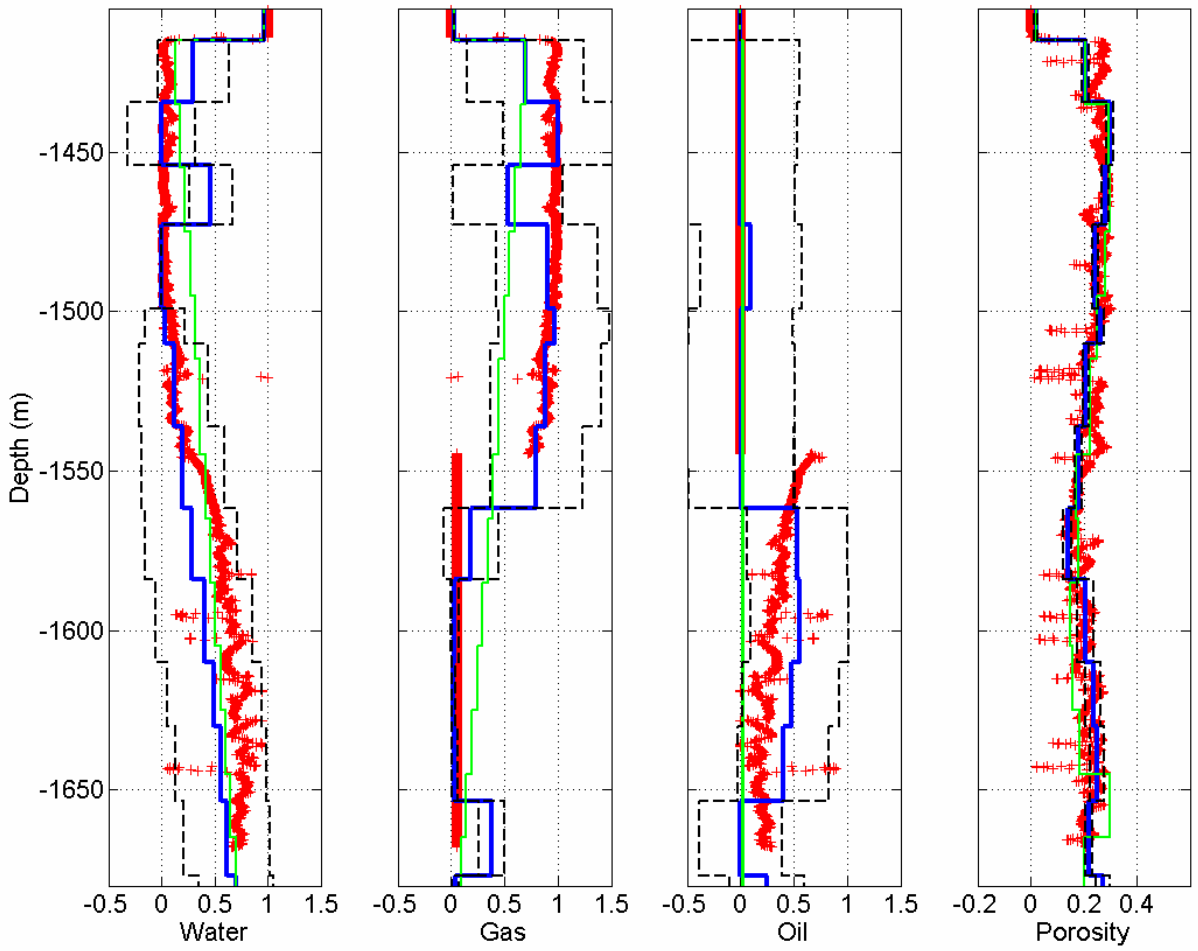

Figure 17. Inversion for water (left panel), gas (second from left), oil (second from right), and porosity (right panel), using both seismic AVA and CSEM data. Red plus signs are log values, green line is parameter values after first iteration when smoothing has flattened the starting model, blue line is final inversion parameters. Black dashed lines are one standard deviation bounds

We note that the S_w levels in this interval (1,550 m to 1,670 m) correspond to S_w levels where V_p is least sensitive to changes in S_w. Figure 19 shows the computed V_p, V_s, and density from the rock-properties model used in the inversion for brine-gas and oil-gas combinations. V_p has a minimum at S_w =0.8, with only small variations between S_w =0.9 and 0.6. The S_w in the lower half of the reservoir interval is mostly in this range. In addition, the V_p and V_s sensitivities to substitution of oil or brine are very small. The differences in V_p, V_s and density between an 80%-20% brine-gas mix and an oil-gas mix of the same ratio is only 1.2%, 1.0% and 2.4% respectively. The insensitivity of the seismic parameters to exchange of oil or brine results in the AVA-only inversion, substituting brine for oil in the lower half of the reservoir. The advantage introduced by adding the CSEM data in the joint inversion is that it serves to constrain S_w. With this added constraint the AVA data can distinguish between oil and gas saturations in the lower

portion of the reservoir. Both AVA-only and AVA-CSEM inversion produce very similar ϕ estimates, the sensitivity to ϕ coming mostly from the AVA data. However, the combined inversion provides lower parameter standard deviations than either CSEM-only or AVA-only inversions.

None of the inversions (CSEM-only, AVA-only, or CSEM-AVA) have resolved the correct location of the GOC at 1544.5 m. The CSEM data by itself does not have the spatial resolution to locate the GOC. The event on the AVA gathers marked T2 in Figures 16 and 18 corresponds to the depth of the GOC and both the AVA-only and the CSEM-AVA inversions have matched this portion of the AVA data. Examination of the velocity and resistivity logs show that there is a smooth transition in velocity and resistivity through the oil zone from the GOC into the paleo-oil-zone. Surrounding hard streaks and porosity changes produce larger variations in velocity (and reflection coefficients) in this portion of the reservoir than that caused by the GOC. Based on the resistivity and velocity logs we believe that the transition in S_g at the GOC is not as sharp as indicated in the calculated S_g and S_o logs shown in Figures 15 and 17 and that the inversion results reflect this fact.

The CSEM data misfit is visually identical to that shown in Figure 15 for the CSEM data only inversion. The slight increase in the data misfit for the AVA-CSEM inverse compared to the AVA-only misfit (0.91 compared to 0.87) is due entirely to an increase in the CSEM data misfit in the joint inversion. We find that as the AVA-CSEM inversion iterations progress the CSEM data is fit first by the relatively smooth (high λ) models. As the iterations increase and λ decreases, admitting rougher models, the AVA data misfit decreases and the CSEM data misfit increases. Inconsistencies between the AVA and CSEM rock-properties models and differences in the spatial sensitivity of the two data sets are two likely sources of decreased data fit in the joint inversion.

Table 2. Numerical measures of fit between the inversion estimates of fluid saturations (Sw, Sg and So) and ϕ compared to the 31/2-1 well logs. Log net S_w = 632, S_g = 831, S_o =262, ϕ =369. The difference between the estimated and logged net values in the reservoir are annotated as Δ.

	S_w RMS	S_w L1	ΔS_w	S_g RMS	S_g L1	ΔS_g	S_o RMS	S_o L1	ΔS_o	ϕ RMS	ϕ L1	$\Delta\phi$
CSEM	**0.15**	**192**	104	na	na	na	na	na	na	0.045	60	18
AVA	0.27	356	**86**	0.38	459	131	0.23	459	218	0.049	67	13
Joint	0.21	292	97	**0.25**	**271**	**42**	**0.2**	**271**	**50**	**0.044**	**57**	**5**

Table 2 shows the numerical measures for the agreement between the inversion estimates of fluid saturations and ϕ compared to the logs. The lowest values (best) are highlighted in bold type. The joint inversion produces the lowest RMS and L1 norm fit to the S_g, S_o and ϕ logs as well as net S_g, S_o and ϕ closest to the log over the reservoir interval. The CSEM inversion

produces the lowest RMS and L1 norm fit to S_w. The AVA-only inversion produces the lowest net S_w over the reservoir interval, slightly better than the CSEM-only inversion.

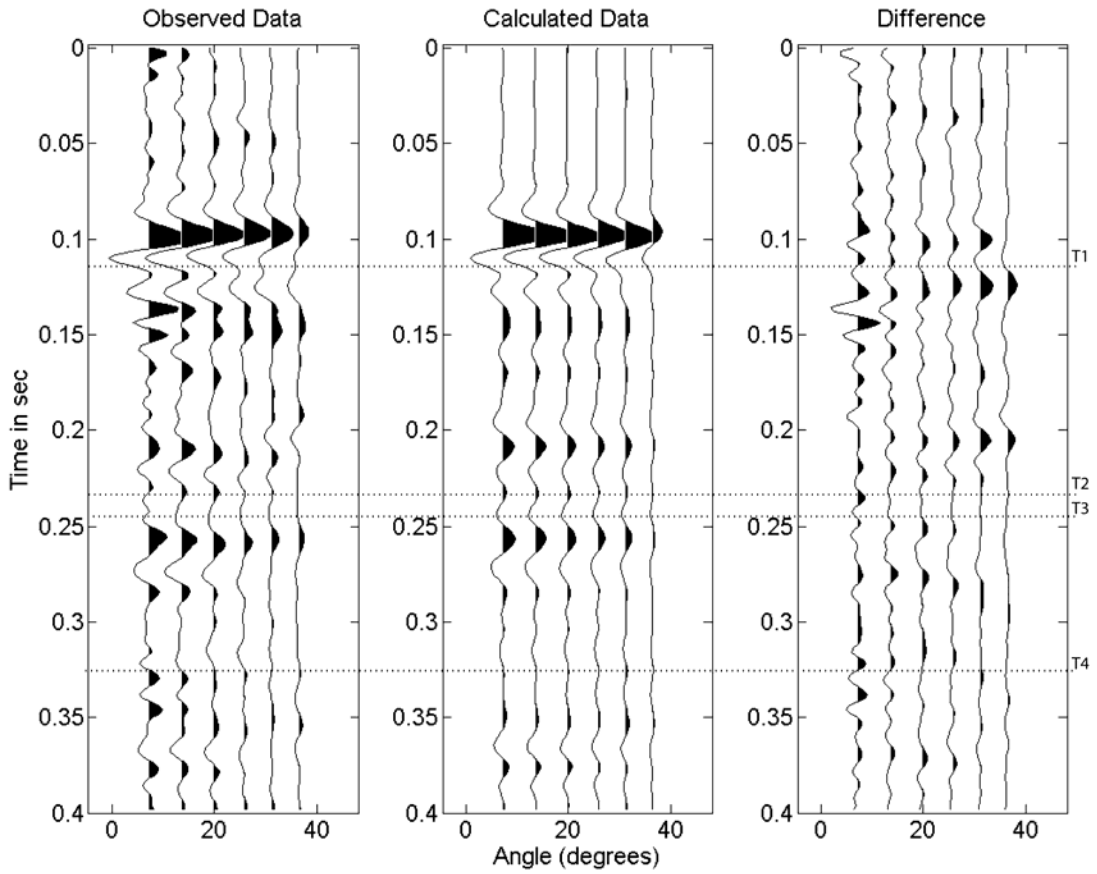

Figure 18. Observed seismic AVA gather (left panel), AVA data calculated from joint seismic and EM inversion model shown in Figure 17 (middle panel), and difference between observed and calculated AVA data (right panel). Zero time corresponds 1300 m depth. Times marked as T1, T2, T3, and T4 on right side of figure correspond to top of gas, gas-oil contact, top of paleo-oil zone and bottom of logged interval respectively. The RMS data misfit is 0.91.

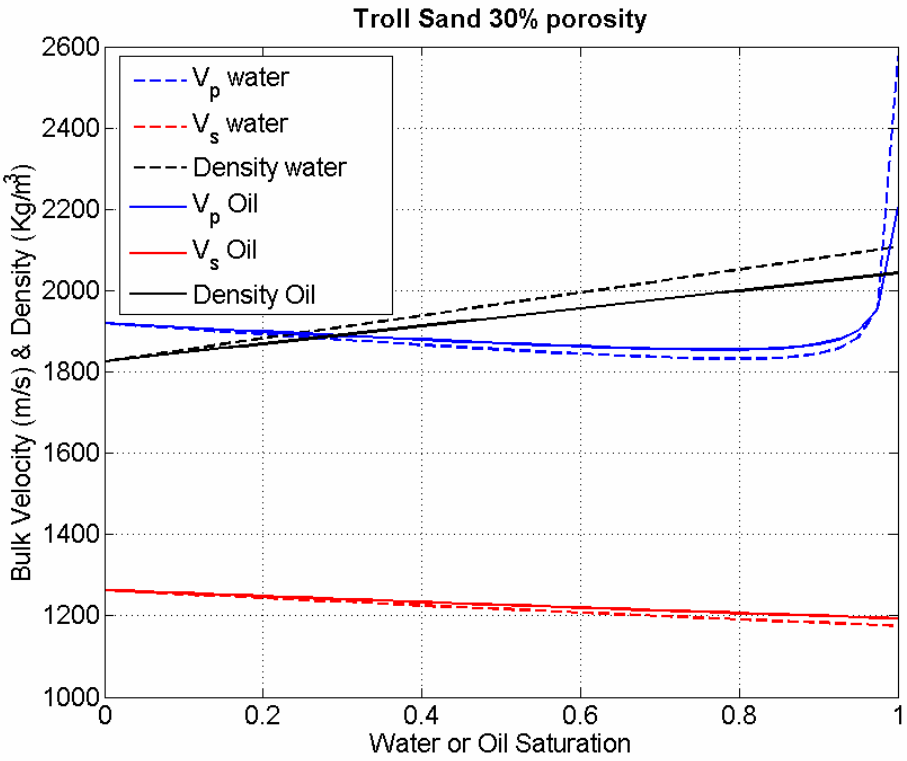

Figure 19. Reservoir bulk acoustic (blue), shear (red) velocity and density (black) calculated as a function of water or oil saturation using the rock properties model derived from logs and used in the inversions shown in Figures 15 and 17.

Discussion and Conclusions

We have developed an algorithm for joint AVA and CSEM inversion. Tests on synthetic 1D models representing gas and petroleum reservoir scenarios show that combining AVA and CSEM data in an inversion for reservoir parameters produces better estimates, with lower variance, compared to either CSEM or AVA inversions done separately. Analysis of error propagation through the rock-properties model shows that errors in the rock-properties model parameters introduce errors of comparable size (in terms of percent) in the joint-inversion reservoir parameter estimates. Errors introduced by the rock-properties model can be reduced if laboratory-derived values for the dry-frame bulk modulus can be used (as opposed to computing the dry-frame bulk modulus from the nonlinear relations of the Hertz-Mindlin model). Field data inversion results from the North Sea Troll Field are consistent with synthetic model results. Estimated gas and oil saturation and porosity from joint inversion are closer to the logged values by all numerical measures, than either CSEM or AVA inversion done separately. The CSEM-only inversion produces a better comparison to logged values for water saturation.

The benefits of combining CSEM data with AVA are more striking in synthetic tests than in the field-data example presented here, although the joint inversion of field data does produce

closer agreement with logged values of S_g, S_o, and porosity with lower parameter standard deviations, than does inversion of either type of data done in isolation. Part of the difference between the performance of the joint inversion on synthetic and field data is certainly a result of the large number of unknown noise sources inherent in the field data. These include noise in the estimated angle-dependent wavelets and the possible presence of correlated (non-Gaussian) noise in both CSEM and AVA data sets. The saturation and porosity logs themselves, assumed as ground truth, can be in error. In addition, the 1D model may not accurately represent the actual earth. This is more likely to be a problem for the CSEM data (which has a larger spatial footprint) than it is for the AVA modeling, although the assumption that all multiples have been removed and that true relative amplitudes have been recovered in the seismic data may also not be strictly valid.

Many of the assumptions inherent in the algorithms presented here can be overcome by increasing the complexity of both the seismic and CSEM models. The next improvement to be investigated would be the use of a 1D elastic seismic calculation that would include all multiples, mode-conversions, and waveform spreading. The CSEM calculation will move from 1D to 3D. Both of these require significantly more computer time, with the 3D CSEM calculations dominating the computing budget and requiring implementation for parallel cluster computing. This work is currently under way. It is also worth considering different types of seismic data for combination with CSEM. In particular, seismic travel-time tomography may provide a better (certainly different) companion for CSEM data, in that the spatial scale of resolution would be more comparable.

The limitations described above notwithstanding, there is benefit to be derived from combining CSEM with seismic data through joint inversion. We hope that this work will stimulate others to pick up the investigation.

Acknowledgments

Support for this work was provided by the Assistant Secretary for Fossil Energy, through the National Energy Technology Laboratory under U.S. Department of Energy under Contract No. DE-AC03-76SF00098. We are grateful to our industry partners (EMGS, StatOil and Shell) for their contributions of data and consultations. In particular, we thank Jaap Mondt and Maren Kleemeyer of Shell and Rune Mittet of EMGS. In addition, we thank the Troll partners (Norsk Hydro, Statoil, Petoro, Norske Shell, Total, and ConocoPhillips) for permission to publish this work.

References

Aki, K., and Richards, P. G., 1980, Quantitative Seismology: Theory and Methods: W. H. Freeman and Co.

Archie, G. E., 1942, The electrical resistivity log as an aid in determining some reservoir characteristics: Trans. Am. Inst. Mech. Eng., **146**, 54-62.

Batzle, M. and Wang, Z., 1992, Seismic properties of pore fluids: Geophysics, **57**, 1396-1408.
Buland, A., and More, H., 2003, Bayesian linearized AVO inversion: Geophysics, **68**, 185-198.
Buland, A., Landro, M., Andersen, M., and Dahl, T., 1996, AVO inversion of Troll Field Data: Geophysics, **61**, 1589-1602.
Castagna, J. P., AVO Analysis – Tutorial and Review, 1993, in Offset-Dependent Reflectivity – Theory and Practice of AVO Analysis., J. P. Castagna and M. M. Backus eds, Investigations in Geophysics no. 8, Soc. of Exp. Geophysics, pp. 3-36.
Constable, S. C., Parker, R. L. and Constable, C. G., 1987, Occam's inversion - A practical algorithm for generating smooth models from electromagnetic sounding data: Geophysics, **52,** 289-300.
Constable, S. C., 1990, Marine electromagnetic induction studies: Surv. Geophys., **11**, 303-327.
Constable, S., Orange, A., Hoversten, G. M., and Morrison, H.F., 1998, Marine Magnetotellurics for petroleum Exploration Part 1: A seafloor equipment system: Geophysics, **63**, 816-825.
Constable, S. C., Parker, R. L. and Constable, C. G., 1987, Occam's inversion - A practical algorithm for generating smooth models from electromagnetic sounding data: Geophysics, **52,** 289-300.
Constable, S., and Cox, C. S., 1996, Marine controlled source electromagnetic sounding 2. The PEGASUA experiment: J. Geophys. Res., **101**, 5519-5530.
Debski, W. and Tarantola, A., 1995, Information on elastic parameters obtained from the amplitudes of reflected waves: Geophysics, **60,** 1426-1436.
Drufuca, G., and Mazzotti, A., 1995, Ambiguities in AVO inversion of reflections from a gas sand: Geophysics, **60**, 134-141.
Dvorkin, J., and Nur, A., 1996, Elasticity of high-porosity sandstones: Theory for two North Sea datasets: Geophysics, **61**, 1363-1370.
Ellingsrud, S., Eidesmo, T., Johansen, S., Sinha, M.C., MacGregor, L. M., and Constable, S., 2002, Remote sensing of hydrocarbon layers by seabed logging (SBL): Results from a cruise offshore Angola: The Leading Edge, **21**, 972-982.
Filloux, J. H., 1983, Seafloor magnetotelluric soundings in the Mariana island arc area, *in* Hayes, D. F., Ed., Tectonic and Geologic Evolution of Southeast Asian Seas and Islands, Part 2: Am. Geophys. Union Geophysical monograph **27**, 255-265.
Fletcher, R., and Jackson, M. P., 1974, Minimization of a quadratic function of many variables subject only to lower and upper bounds: J. Inst. Math. Applics., **14**, 159-174.
Hashin, Z., and Shtrikman, S., 1963, A variational approach to the elastic behavior of multiphase materials: J. Mech. Phys. Solids, **11**, 127–140.
Hoversten, G. M., and Unsworth, M. , 1994, Subsalt imaging via seaborne electromagnetics, Offshore Technology Conference, Houston, TX. Vol. **26**, Vol. 1 p. 231-240.
Hoversten, G. M., Morrison, H.F., and Constable, S., 1998, Marine magnetotellurics for petroleum exploration Part 2: Numerical analysis of subsalt resolution: Geophysics, **63**, 826-840.
Hoversten, G. M., Constable, S. C., and Morrison, H. F., 2000, Marine magnetotellurics for base salt mapping: Gulf of Mexico Field Test at the Gemini Structure: Geophysics, **65**, 1476-1488.

Hoversten, G. M., Newman, G. A., Morrison, H.F., Gasperikova, E., and Berg, J. I., 2001, Reservoir characterization using crosswell EM inversion: A feasibility study for the Snorre Field, North Sea: Geophysics, **66**, 1177-1189.

Hoversten, G., M., Gritto, R., Washbourne, J., and Daley, T. M., 2003, Pressure and fluid Saturation prediction in a multicomponent reservoir, using combined seismic and electromagnetic imaging: Geophysics, **68**, 1580-1591.

Hwang, L. -F. and McCorkindale, D., 1994, Troll field depth conversion using geostatistically derived average velocities: The Leading Edge, **13**, 262-269.

Landro, M., 2001, Discrimination between pressure and fluid saturation changes from time-lapse seismic data: Geophysics, **66,** 836-844.

Levy, S. and Fullagar, P. K., 1981, Reconstruction of a sparse spike train from a portion of its spectrum and application to high-resolution deconvolution: Geophysics, **46,** 1235-1243.

Lumley, D., Meadows, M., Cole, S. and Adams, D., 2003, Estimation of reservoir pressure and saturations by crossplot inversion of 4D seismic attributes, 73rd Ann. Internat. Mtg.: Soc. of Expl. Geophys., 1513-1516.

Mindlin, R. D., 1949, Compliance of elastic bodies in contact, Trans. ASME, **71**, A-259.

Newman, G. A., and Alumbaugh, D. L., 1997, Three-Dimensional massively parallel electromagnetic inversion-I. Theory: Geophys. J. Int., **128**, 345-354.

Newman, G. A., and Hoversten, G. M., 2000, Solution strategies for two- and three-dimensional electromagnetic inverse problems: Inverse Problems, **16**, 1357-1375.

Plessix, R. -E., and Bork, J., 2000, Quantitative estimate of VTI parameters from the AVA responses: Geophys. Prosp., Eur. Assn. Geosci. Eng., **48,** 87-108.

Spies, B. R., 1989, Depth of investigation in electromagnetic sounding methods: Geophysics. **54**, 872-888.

Tarantola, A., 1987, Inverse Problem Theory: Methods for Data Fitting and Model Parameter Estimation: Elsevier.

Tikhonov, A. N., and Arsenin, V. Y., 1977, Solutions to Ill-posed Problems, John Wiley and Sons, Ndew York, NY.

Tura, A. C., and Lumley, D., 1999, Estimating pressure and saturation changes from time-lapse AVO data, 69th Ann. Internat. Mtg: Soc. of Expl. Geophys., 1655-1658.

Ward, S. H., and Hohmann, G. W., 1987, Electromagnetic Theory for Geophysical Applications, In: Nabighian, M. N. (ed.), Electromagnetic Methods in Applied Geophysics, Vol. 1, Theory, SEG Investigations in geophysics, no3, 131-228.

Xie, G., Sen, M. K., and Stoffa, P. L., 2000, Mapping of elastic properties of gas hydrates in the Carolina trough by waveform inversion. Geophysics, **65**, 735-744.